

PAPER

A simulation-based study on the influence of the x-ray spectrum on the performance of multi-material beam hardening correction algorithms

To cite this article: Wenchao Cao *et al* 2018 *Meas. Sci. Technol.* **29** 095002

View the [article online](#) for updates and enhancements.

Related content

- [A fast beam hardening correction method incorporated in a filtered back-projection based MAP algorithm](#)
Shouhua Luo, Huazhen Wu, Yi Sun et al.
- [Segmentation-free statistical image reconstruction](#)
Idris A Elbakri and Jeffrey A Fessler
- [Patient-specific scatter correction for flat-panel detector-based cone-beam CT imaging](#)
Wei Zhao, Stephen Brunner, Kai Niu et al.



IOP | ebooks™

Bringing you innovative digital publishing with leading voices to create your essential collection of books in STEM research.

Start exploring the collection - download the first chapter of every title for free.

A simulation-based study on the influence of the x-ray spectrum on the performance of multi-material beam hardening correction algorithms

Wenchao Cao¹, Tao Sun², Greet Kerckhofs³, Gemma Fardell⁴, Ben Price⁴ and Wim Dewulf¹

¹ Department of Mechanical Engineering, KU Leuven, Celestijnenlaan 300, 3001, Leuven, Belgium

² Department of Nuclear Medicine & Molecular Imaging, KU Leuven, UZ Herestraat 49, 3000, Leuven, Belgium

³ Biomechanics lab, Institute of Mechanics, Materials, and Civil Engineering, Universit Catholique de Louvain, Louvain-la-Neuve, Belgium

⁴ X-Tek Systems Ltd (Nikon Metrology UK Ltd), Unit 5, Icknield Industrial Estate, Tring, United Kingdom

E-mail: wenchao.cao@kuleuven.be

Received 20 March 2018, revised 27 May 2018

Accepted for publication 11 June 2018

Published 23 July 2018



Abstract

Beam hardening artefacts caused by the polychromatic nature of the x-ray spectra are known to deteriorate the reconstructed image quality in multi-material industrial computed tomography. A variety of beam hardening correction (BHC) algorithms exist. Most of these methods rest on the x-ray spectra to a certain extent, which means their performance may be hindered if the spectral information is not accurate. The dependence of these methods on the spectral information, however, has not been benchmarked. This work addresses the need for such investigation by applying two sets of spectra—(1) a set of the true spectra used to produce the radiography, and (2) a set of approximated spectra acquired from simulation—to three multi-material BHC algorithms of different types. The algorithms are a segmentation based linearisation algorithm, a dual-energy algorithm, and an iterative reconstruction algorithm. Our objective in this study is to estimate the dependence of these three algorithms on spectral information. For comparable accuracy, multiple metrics are employed to quantify the performance of the methods in terms of artefact presence and dimensional metrology. The results show that under the same initial conditions, dual-energy appears to be the most sensitive one to the spectral change. Contrariwise, the segmentation method is least spectrally sensitive. The iterative method is stable over the spectral change, but performs poorly in dimensional metrology.

Keywords: x-ray spectral analysis, beam hardening, dimensional metrology, x-ray CT

(Some figures may appear in colour only in the online journal)

1. Introduction

X-ray computed tomography (CT) is a promising imaging modality in industrial inspection and metrology for its non-contact and non-destructive nature. There are several artefacts

that impair the image fidelity to the object being scanned, chief among which is beam hardening (Herman 2009). Beam hardening artefacts stem from the fact that the x-ray spectrum extends over a broad range of energies (polychromatic) and the attenuation coefficients are energy-dependent (Bushberg

and Boone 2011). Conventional CT detectors are energy insensitive. They record x-ray photon transmission through a sample. This information is then reconstructed with a certain algorithm for a 3D image. In the conventional filtered back projection (FBP) reconstruction algorithm, the x-ray spectrum is assumed to be mono-energetic. The relationship between the transmitted x-ray beam intensity I after passing through a single material and the incident beam intensity I_0 is therefore modelled as

$$-\ln\left(\frac{I}{I_0}\right) = p_m = \int \mu(x, y) dl \quad (1)$$

where p_m stands for the logarithmic monochromatic projection value, and $\mu(x, y)$ is the attenuation coefficient at position (x, y) , which is a function of the propagation length l at given energy.

In reality, the logarithmic transmission is modelled as

$$\begin{aligned} -\ln\left(\frac{I}{I_0}\right) &= p_p \\ &= -\ln\left(\frac{\int I(E)\exp(-\int \mu(x, y, E)dl)\gamma(E)dE}{\int I(E)\gamma(E)dE}\right) \\ &= -\ln\left(\frac{\int S(E)\exp(-\int \mu(x, y, E)dl)dE}{\int S(E)dE}\right) \end{aligned} \quad (2)$$

where p_p is the logarithmic polychromatic projection value, $\mu(x, y, E)$ is the attenuation coefficient at position (x, y) with energy E , which is a function of both the propagation length and energy. $\gamma(E)$ is the quantum detection efficiency, $S(E)$ is the product of the x-ray spectrum and the quantum detection efficiency and its integral is equal to 1. Beam hardening artefacts result from ignoring $S(E)$ in the FBP algorithm.

The state-of-the-art beam hardening correction (BHC) algorithm used in most commercial industrial CT software packages is linearisation (Herman 1979). It fails with multi-material objects essentially because it is based on a one-to-one mapping between mono- and poly-energetic measurements. More advanced BHC algorithms which are capable of correcting multi-material objects have drawn a lot of attention recently. They can roughly be divided into three categories based on their principal methodologies—namely, dual-energy (Alvarez and Macovski 1976, Fessler *et al* 2002, Zhang *et al* 2014), multi-material linearisation (Joseph and Spital 1978, Herman and Trivedi 1983, Meagher *et al* 1990, Joseph and Ruth 1997, Hsieh *et al* 2000, Krumm *et al* 2008, Lifton 2017), and iterative methods (De Man *et al* 2001, Brabant *et al* 2012, Van Slambrouck and Nuyts 2012).

The spectral information plays a crucial role in the beam hardening correction algorithms mentioned above. There are three approaches to obtaining the spectral information: spectral simulation (Siewerdsen *et al* 2004, Poludniowski *et al* 2009), spectrometer measurements (Birch and Marshall 1979, Miyajima *et al* 2002), and attenuation measurements (Sidky *et al* 2005, Duan *et al* 2011, Lin *et al* 2014, Leinweber *et al* 2017). Spectral measurements are not practical for every acquired CT scan. In the absence of direct measurements, the closest spectra we can get are either simulated based on the

technical specifications of a CT system or manufacturer provided. Therefore, a mismatch between the spectral input to the algorithm and the actual spectra of the physical CT system is inevitable.

Researchers have been actively working on addressing this issue. A well-known solution is material calibration (Abella and Fessler 2009), which involves scanning phantoms with known material and geometry. These calibration data are only applicable to the same CT system settings, energy levels, and sample materials. The spectral information can be considered as enclosed in the calibration scans. This method is appropriate for users who need to repeatedly scan samples of the same materials (or at least materials with similar densities). However, the scope of application is limited. There are also some published studies describing BHC algorithms that do not require spectral information (de Castele *et al* 2004, Krumm *et al* 2008). These methods normally embark on a quasi-material calibration step in the sample scan. That is to say, the material and x-ray propagation length information of the sample is learned from a preliminary FBP reconstruction. The regions belonging to different materials in the reconstructed volume are arbitrarily segmented, and the x-ray propagation lengths are acquired with ray-tracing (Joseph 1982, Jacobs *et al* 1998). This somewhat self-contained material calibration has an obvious inherent shortage—not all the materials are distinguishable with the presence of beam hardening. These methods are, therefore, not always guaranteed to work.

Compared with the popularity of the BHC research, where in recent years numerous papers have been devoted to novel algorithms that attempt to avoid spectral knowledge, there is a lack of in-depth study regarding the dependence of the more established algorithms on the spectral knowledge. Therefore, the objective of this study is to investigate the sensitivity of these methods to the uncertainty on the applied spectra.

As discussed before, multi-material BHC algorithms fall into three categories. We chose one classic method from each category for comparison, since methods in the same peer category share similar physical and mathematical principles. The methods investigated are Joseph segmentation (Joseph and Spital 1978), Alvarez dual-energy (Alvarez and Macovski 1976), and IMPACT iterative (De Man *et al* 2001). These methods are well defined in the physical model, applicable across diverse data conditions and sizes, and flexible with respect to modification. Therefore, they have the most potential to be applied in industry. Although there are newer publications based on these methods, they are mostly modified for specific applications or improving the processing speed. Some approaches (Gao *et al* 2006, Van Slambrouck and Nuyts 2012) have applied BHC only to the metal part of the object, to reduce the processing time. There are also approaches (de Castele *et al* 2004, Brabant *et al* 2012) designed for scanning under low energy range. To cover a wide range of possible applications in industrial CT, we chose to use classical methods.

We exploited a simulation framework that incorporates experimentally measured spectra. Simulation was used because, firstly, with simulation, we can exclude other artefact

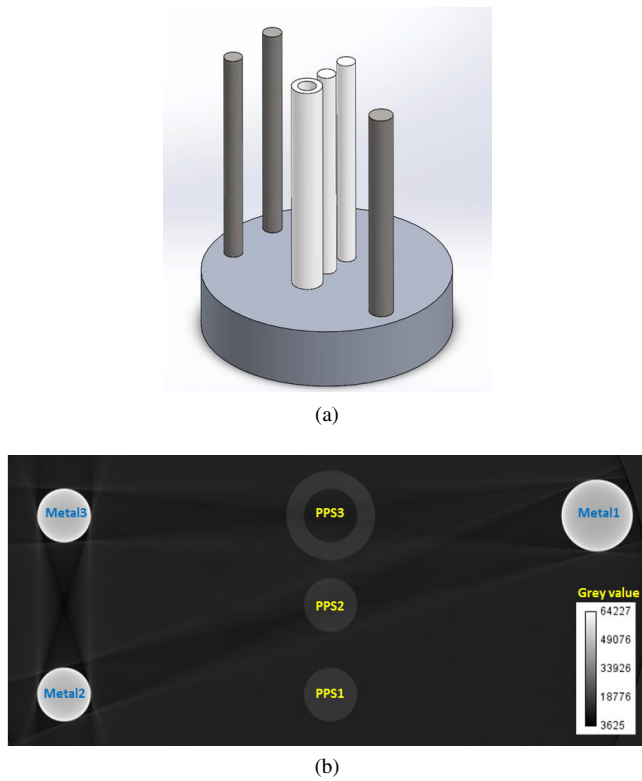


Figure 1. Virtual phantom. (a) A 3D drawing of the phantom. Various Al and PPS rods are inserted into the plastic plate. Al is labeled in dark grey, and PPS is labeled in light grey. PPS₃ provides both external and internal features to study. (b) Reconstructed central slice of the simulated phantom.

Table 1. Phantom element nominal dimensions.

Phantom element	Nominal radius (mm)
Al1	1.5
Al2	2.0
Al3	1.5
PPS1	1.5
PPS2	1.5
PPS3—external	2.5
PPS3—internal	1.5

mechanisms, so that our evaluation is able to recognise the performance of an algorithm with respect to beam hardening alone. Secondly, it allows us to incorporate measured spectra in the projection process of this study.

2. Materials and methods

2.1. Virtual phantom

A multi-material virtual phantom is designed for the simulation framework of this study. The phantom comprises three metal rods, two solid plastic rods, and one hollow plastic rod. The metal material is aluminium (Al), and the plastic material is polyphenylene sulphide (PPS). The phantom features multiple external and internal dimensions (figure 1). Details of the phantom geometry are given in table 1. This phantom configuration has been introduced in Cao *et al* (2018).

2.2. X-ray spectral measurements

In order to obtain realistic results, the simulations were performed based on spectra from an existing CT system. One pair of spectra (the measured true spectra) were used for the simulation of the dataset, whereas the algorithms were then run with a different pair of spectra (the approximated spectra). The spectra used in this study were measured 50 kVp and 70 kVp spectra from a Skyscan 1172 CT machine that was available at KU Leuven from former research (Kerckhofs 2009). A portable apparatus was used together with dedicated software to perform a direct spectral reconstruction of the radiation produced by the x-ray tubes (Stumbo *et al* 2004). Briefly, for different tube voltages and tube currents, the number of events (i.e. detections of single photons or pile-ups of photons with similar energy) was measured at the detector for each photon energy within a given time period, and the total number of photons per photon energy and per second (i.e. flux) was calculated. The detector system directly calculated the number of incident photons and the spectrum of the tube. Monte Carlo reconstruction of the emitted spectra was conducted by dedicated software. In this way, the full shape and temporal position of each pulse were recorded. The acquisition system was a commercially available CZT (Cadmium–Zinc–Tellurium) solid-state detector ($3 \times 3 \times 2$ mm), with a $250 \mu\text{m}$ thick Beryllium window (AMPTeK Inc., Bedford, USA) and a high efficiency in the diagnostic x-ray energy range. The typical energy resolution was $<1.5\text{ kV}$ full width at half maximum (FWHM). To reduce the flux to values accepted by the system, the detector was collimated via a tungsten disk with a circular hole.

A 0.5 mm Al filter was applied to the tungsten (W) target source for the measured spectra. The measured spectra were down-sampled to 1 kV by summing up the photon counts in each energy interval E in the range $(E - 1/2, E + 1/2)$, and then normalised for the following experiments. A corresponding pair of approximated spectra was simulated (Poludniowski *et al* 2009) according to the specifications of this system. The root mean square deviations (RMSDs) between the true and approximated spectra were 0.0036 and 0.0056 respectively (figure 2). The projection images were simulated using the true spectra. The datasets were processed with the BHC algorithms both with the approximated spectra and the true spectra for reference, and the artefact reduction and dimensional accuracy were compared.

Although the x-ray tube spectra were measured with a photon counting detector, the task detector efficiency remained a source of uncertainty. Because the task detector used for scanning was different from the one for spectral measurements, it was impossible to determine the efficiency of the task detector. Even if the theoretical efficiency was provided by the manufacturer, the true efficiency of a specific detector deviated over time.

2.3. Assessment metrics

2.3.1. Streak index. The artefact reduction indices, which include streak index (SI) and cupping effect index (CI),

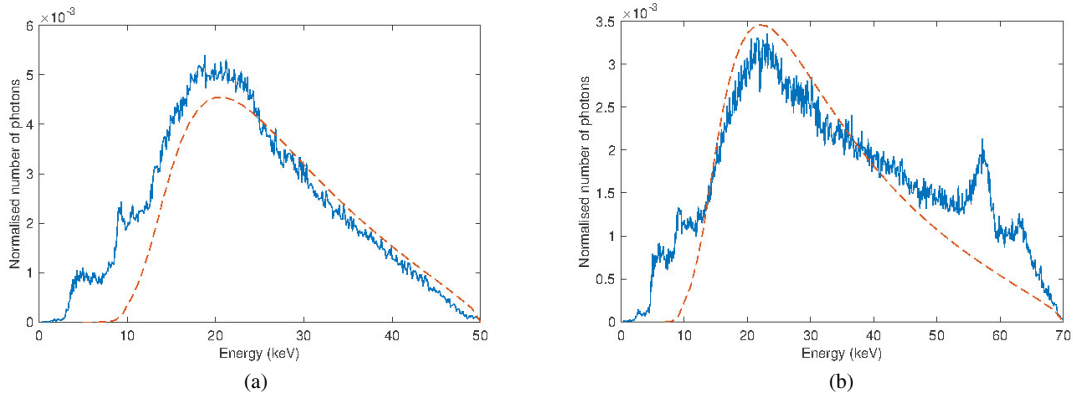


Figure 2. The spectra used: (a) 50 kVp, (b) 70 kVp. The true spectra are shown in blue, and the approximated spectra in red.

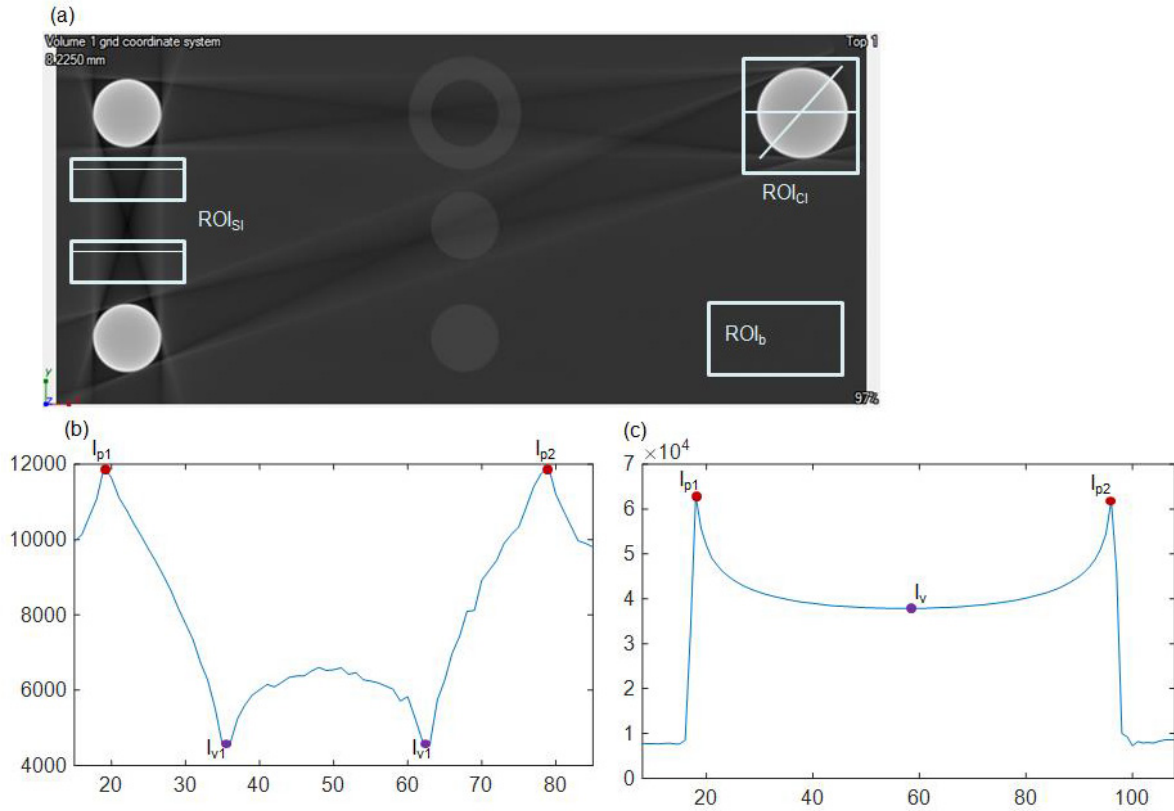


Figure 3. (a) ROI definitions of the assessment metrics. Within each ROI_{SI} and ROI_{CI}. For clarity, only two are shown. (b) A SI line profile. The peaks and valleys correspond to the bright and dark streaks that the line traverses. (c) A CI line profile. The peaks and valley correspond to the edge and centre of the rod that the line traverses.

were initially introduced in Cao *et al* (2018) as a tool to assess the beam hardening artefact reduction in the reconstructed image. The SI metric quantifies the grey value change caused by beam hardening streaks between the rods. The regions of interest (ROIs) and line profiles are shown in figure 3. ROI_{SI} are the two rectangles for SI calculation. Each rectangle is 45×94 pixels. They include line profiles with two bright and two dark streaks. A total of 90 lines are drawn in ROI_{SI}.

The following formulas are used for the calculation:

$$I_a = \frac{I_{p1} + I_{p2}}{2} \quad (3)$$

$$I_b = \frac{I_{v1} + I_{v2}}{2} \quad (4)$$

$$SI = \frac{1}{n} \times \sum_{i=1}^n \frac{I_{ai} - I_{bi}}{\max(I_{ai}, I_{bi}) - M_b + C} \quad (5)$$

where I_{p1} and I_{p2} are the two grey value peaks, and I_{v1} and I_{v2} are the two grey value valleys. I_a and I_b are the corresponding averages. M_b is the average grey value of ROI_b. C is the biggest grey value of a 16-bit image, which equals 65535. Its value varies between -1 and 1 , and is 0 in the absence of beam hardening. Notice that the pixel indices of I_{p1} and I_{p2} are

Table 2. Specifications of the aRTist simulation.

Source type	Reflection, tungsten target
Voltage range	Monochromatic: 28 kV Polychromatic: 50–70 kVp
Focal spot	Point
Source to object distance	250 mm
Source to detector distance	1000 mm
Projection number	3600
Detector	0.2 mm pixel size, 2000 × 2000 pixels, 16-bit dynamic range, energy-summing flat panel

determined only on the uncorrected images, and subsequently applied to all the corrected images. When the image is not corrected, the SI value is always positive. It is only negative when over-correction (i.e. peaks and valleys swap) happens.

2.3.2. Cupping effect index. The CI metric quantifies the grey value change caused by the cupping effects at the boundary of the rod. The ROIs and line profiles are shown in figure 3. On the rod in ROI_{CL}, a total of 180 lines are used for CI calculation. Each of them extends 0.25 mm outside the rod in both directions.

The following formula is used for the calculation:

$$CI = \frac{1}{n} \times \sum_{i=1}^n \frac{I_{ai} - I_{bi}}{\max(I_{ai}, I_{bi}) - M_b + C}. \quad (6)$$

The notations are the same as those described in section 2.3.1, yet since each line profile comprises only one valley, I_b equals I_v .

To avoid cone-beam artefacts, only the reconstructed slice located in the central cone plane is used for SI and CI calculation. The values may vary if other slices close to the centre are used because of the systematic noise introduced in reconstruction. However, this is negligible compared to the grey value change caused by beam hardening.

2.3.3. Dimensional measurements. CT metrology is a recent metrological advance. Its advantage lies in its ability of non-destructive measurement of the internal features. The mechanism of how the BHC algorithms affect the dimensional properties of the phantom needs to be understood, because it determines the reliability of CT as a technique for metrology.

The dimensional measurement errors compared to the reference measurements are calculated by

$$\text{Error } (\mu\text{m}) = \text{reference radius} - \text{measured radius}$$

The corresponding monochromatic dataset is used for dimensional measurement reference values. The simulation process inevitably causes errors; thus, the real dimension of the phantom will never be equal to its nominal value. A near-optimal solution is to use the measurement from the monochromatic dataset as the reference.

The measurement is performed in VGStudio MAX 2.2.6 (Volume Graphics, Germany) by fitting a cylinder to the determined surface using the least-squares geometry fitting algorithm. To minimise the effect of cone-beam artefacts, only the middle third of the rod is used for dimensional measurement.

The surface determination is performed using the ‘advanced mode’ in VGStudio, with a search distance of 0.2 mm (which is equivalent to four voxels).

2.4. Simulation and data processing

The phantom projections were simulated with aRTist software (Bellon and Jaenisch 2007) under various energy settings. The specifications of the simulation can be found in table 2. No quantum noise or scattering was simulated, to exclude those factors which could be mistaken for beam hardening. The spectral simulation was conducted with SpekCalc (Poludniowski *et al* 2009) with 1 kV energy interval. FBP reconstructions were conducted with CTPro (X-Tek Systems Ltd., Tring, UK). The phantom element dimensions were measured in VGStudio MAX 2.2.6. The results of dual-energy and segmentation methods were based on the FBP reconstructed datasets. FBP reconstruction was not needed for the datasets acquired from the iterative method, as it is a self-contained reconstruction algorithm. The dual-energy and segmentation methods were implemented in MATLAB R2015a on a laptop computer with 8 GB RAM and a 2.5 GHz quad-core processor. The dual-energy method took about 3 h to process one dataset. The segmentation method took about 1.5 h. The iterative method was implemented in IDL on a desktop computer with 32 GB RAM and a 3.6 GHz quad-core processor. It took 6 h to run on a Tesla C2075 GPU.

2.5. Implementation of the algorithms

2.5.1. Dual-energy. The dual-energy method was implemented based on the Alvarez method (Alvarez and Macovski 1976). In the Alvarez method, the attenuation coefficient is formulated as follows:

$$\mu(E) = a_1 f_{\text{PE}} + a_2 f_{\text{KN}} \quad (7)$$

where

$$f_{\text{PE}} = \frac{1}{E^3}$$

$$f_{\text{KN}}(\alpha) = \frac{1 + \alpha}{\alpha^2} \left[\frac{2(1 + \alpha)}{1 + 2\alpha} - \frac{1}{\alpha} \ln(1 + 2\alpha) \right] + \frac{1}{2\alpha} \ln(1 + 2\alpha)$$

and $\alpha = E/510.975$ kV. f_{PE} is the approximate energy dependence of the photoelectric effect, and f_{KN} is the Klein–Nishina function, which gives the energy dependence of Compton scattering cross-section. a_1 and a_2 are two energy independent coefficients.

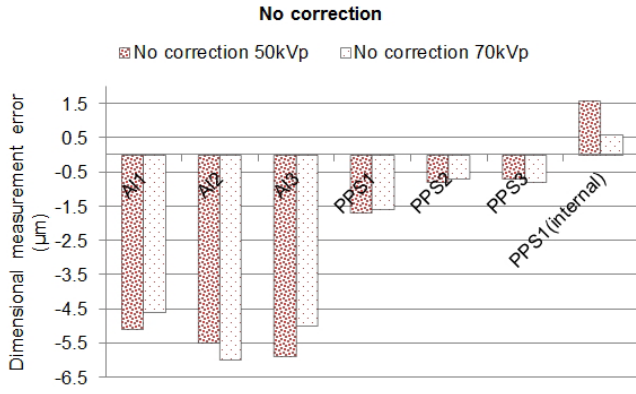


Figure 4. Dimensional measurement errors obtained from uncorrected polychromatic simulations (no correction).

The reconstruction of a_1 and a_2 requires the measurement of line integrals $A_1 = \int a_1 ds$ and $A_2 = \int a_2 ds$ at every pixel in the projections of the object. To obtain A_1 and A_2 , two independent pieces of information must be available at each pixel, which can be done by making measurements at two different energies:

$$I_h = \int S_h(E) \exp[-A_1 f_{PC}(E) - A_2 f_{KN}(E)] dE \quad (8a)$$

$$I_l = \int S_l(E) \exp[-A_1 f_{PC}(E) - A_2 f_{KN}(E)] dE. \quad (8b)$$

S_h and S_l represent the x-ray spectra of the high and low energy measurements, respectively. A_1 and A_2 can be solved using the Newton–Raphson method. The continuous spectra $S(E)$ are represented by the set of discretised values $D(E)$, where

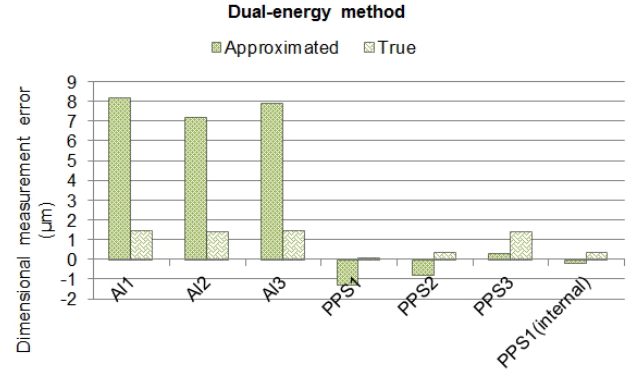
$$D(E) = \int_{E_n - \frac{\Delta E}{2}}^{E_n + \frac{\Delta E}{2}} S(E) dE. \quad (9)$$

ΔE is the width of the energy interval over which the spectra are integrated. In our implementation, ΔE was 5 kV and the low energy cut-off was 4 kV. The monochromatic image was tuned at 28 kV.

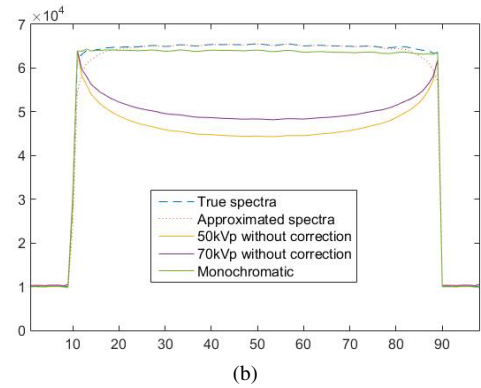
2.5.2. Segmentation. A segmentation based linearisation method was implemented based on the Joseph–Spital method (Joseph and Spital 1978). For a dual-material object with attenuation coefficients denoted by $\mu_1(x, y, E)$ and $\mu_2(x, y, E)$, the polychromatic projection data can be expressed as

$$\begin{aligned} p_p &= -\ln \left(\frac{\int S(E) \exp(-\int \mu_1(x, y, E) dl_1 - \int \mu_2(x, y, E) dl_2) dE}{\int S(E) dE} \right) \\ &= -\ln \left(\frac{\int S(E) \exp(-\int \mu_1(x, y, E) dl_1) dE}{\int S(E) dE} \right) \\ &\quad - \ln \left(\frac{\int S'(E) \exp(-\int \mu_2(x, y, E) dl_2) dE}{\int S'(E) dE} \right) \\ &= p_1 + p_2 \end{aligned} \quad (10)$$

where $S'(E) = S(E) \exp(-\int \mu_1(x, y, E) dl_1)$; p_1 and p_2 are the polychromatic contributions of the metal and plastic materials; l_1 is the propagation length of the metal material.



(a)



(b)

Figure 5. Dual-energy method. (a) Dimensional measurement errors obtained from the simulation using the same spectra for forward projection and for dual-energy BHC (True), and from the simulation using different spectra for forward projection and for dual-energy BHC (Approximated). All errors are defined with respect to the monochromatic simulation. (b) Line profiles along a diameter of rod A1 obtained from the monochromatic simulation, the uncorrected polychromatic simulations, from the simulation using the true spectra for dual-energy BHC, and from the simulation using the approximated spectra.

Table 3. Metric values.

		CI	SI
No correction	50 kVp	0.138	0.092
	70 kVp	0.118	0.075
Dual-energy	True	−0.012	−0.016
	Approximated	−0.021	−0.040
Segmentation	True 50 kVp	6×10^{-3}	0
	Approximated 50 kVp	8×10^{-3}	0
	True 70 kVp	-6×10^{-3}	0
	Approximated 70 kVp	-8×10^{-3}	0
Iterative	True 50 kVp	-2×10^{-3}	0
	Approximated 50 kVp	-6×10^{-3}	0
	True 70 kVp	-2×10^{-3}	0
	Approximated 70 kVp	-6×10^{-3}	0

There are two stages to this method. The first stage involves building up a lookup table (LUT) for the plastic material linearisation. In equation (10), $S'(E)$ is a function of l_1 . We used propagation length from 0 to 9.99 mm with a 0.01 mm interval in the LUT. A four-order polynomial fit was used to linearise p_2 under each $S'(E)$. Therefore, the LUT size was 1000×4 .

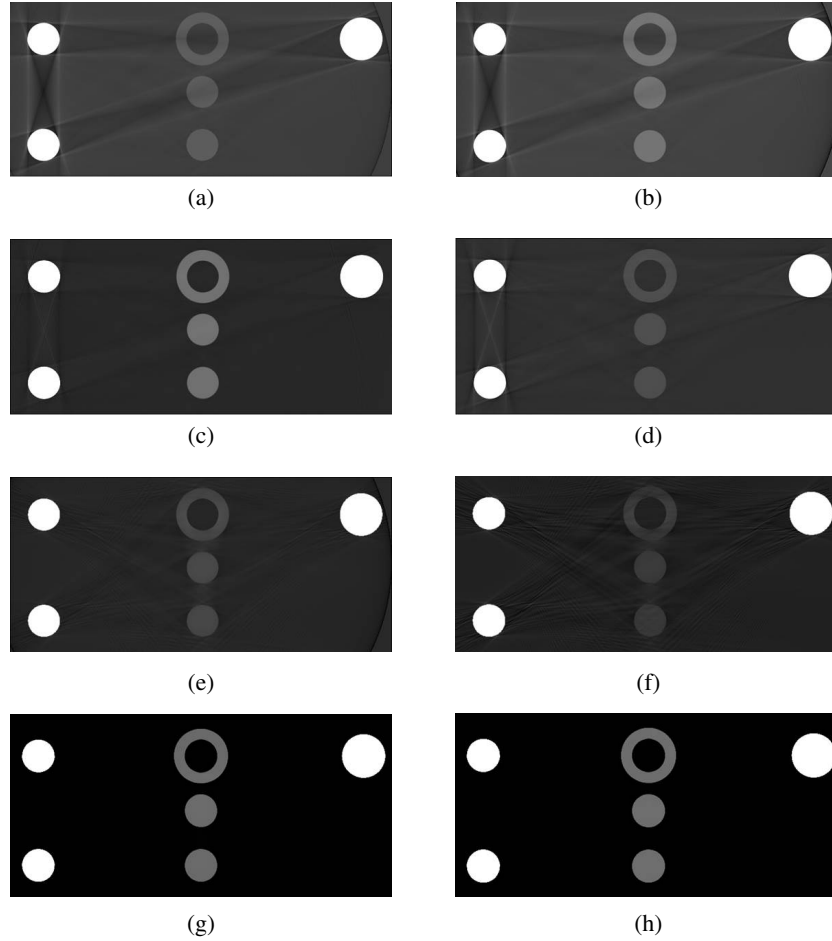


Figure 6. Central slices of the reconstructed images. (a) 50 kVp without correction. (b) 70 kVp without correction. (c) Dual-energy (true spectra). (d) Dual-energy (approximated spectra). (e) Segmentation (true 50 kVp). (f) Segmentation (approximated 50 kVp). (g) Iterative (true 50 kVp). (h) Iterative (approximated 50 kVp).

In the second stage, after initial reconstruction, the metal rods were segmented using the ISO50 value provided by VGStudio MAX 2.2.6. The propagation length corresponding to each pixel was traced using the Siddon algorithm (Siddon 1985). The monochromatic contribution of the metal material was calculated directly with $m_1 = \mu_1(E_0) \times l_1$. The monochromatic tuning energy E_0 was 28 kV. The monochromatic contribution of the plastic material was linearised by the polynomial coefficients in the LUT. Linear interpolation was used to index the LUT.

2.5.3. Iterative method. The iterative method was implemented based on IMPACT (De Man et al 2001).

The polychromatic projection formula is given by

$$\hat{y}_i = \sum_k \hat{y}_{ik} = \sum_k b_{ik} \exp(-\Theta_k \sum_j l_{ij} \theta(\mu_{j,ref}) - \Phi_k \sum_j l_{ij} \phi(\mu_{j,ref})) \quad (11)$$

where l_{ij} is the propagation length of projection line i with pixel j . The attenuation coefficient is decomposed using the Alvarez dual-energy formula. Θ_k and Φ_k are the energy dependence of Compton scattering and photo-electric effect respectively at energy level k . $\mu_{j,ref}$ is the attenuation coefficient at a chosen reference monochromatic tuning energy. We assume that each pixel can be modelled as a mixture of two base substances.

The algorithm updates the following attenuation coefficient:

$$\Delta\mu_j = \frac{\phi'_j \sum_i l_{ij} e_i Y_i^\Phi + \theta'_j \sum_i l_{ij} e_i Y_i^\Theta}{\phi'_j \sum_i l_{ij} M_i + \theta'_j \sum_i l_{ij} N_i} \quad (12)$$

where

$$\phi'_j = \frac{\partial \phi}{\partial \mu_j} \quad \theta'_j = \frac{\partial \theta}{\partial \mu_j}$$

$$e_i = 1 - \frac{y_i}{\hat{y}_i}$$

$$Y_i^\Phi = \sum_k \Phi_k \hat{y}_{ik}$$

$$Y_i^{\Phi\Phi} = \sum_k \Phi_k^2 \hat{y}_{ik}$$

$$Y_i^{\Phi\Theta} = \sum_k \Phi_k \Theta_k \hat{y}_{ik}$$

$$Y_i^\Theta = \sum_k \Theta_k \hat{y}_{ik}$$

$$Y_i^{\Theta\Theta} = \sum_k \Theta_k^2 \hat{y}_{ik}$$

$$M_i = \left(\sum_h l_{ih} \phi'_h \right) \left(Y_i^{\Phi\Phi} e_i + \frac{y_i (Y_i^\Phi)^2}{\hat{y}_i^2} \right) + \left(\sum_h l_{ih} \theta'_h \right) \left(Y_i^{\Phi\Theta} e_i + \frac{y_i Y_i^\Phi Y_i^\Theta}{\hat{y}_i^2} \right)$$

$$N_i = \left(\sum_h l_{ih} \phi'_h \right) \left(Y_i^{\Theta\Theta} e_i + \frac{y_i (Y_i^\Theta)^2}{\hat{y}_i^2} \right) + \left(\sum_h l_{ih} \theta'_h \right) \left(Y_i^{\Theta\Phi} e_i + \frac{y_i Y_i^\Theta Y_i^\Phi}{\hat{y}_i^2} \right).$$

Each update requires eight forward- and back-projections. 50 iterations of 100 subsets were used. The energy interval of the spectrum was 5 kV. The monochromatic tuning energy

was 28 kV. Aluminium and PPS were used as the base substances for the dual-energy decomposition.

Iteratively reconstructed images are often affected by edge artefacts that are not observed in FBP images (Zbijewski and Beekman 2003). Therefore, all the iteratively reconstructed volumes were treated first with a median filter and then a bilateral filter. The purpose of applying post-filtration was to suppress the edge overshoot artefact induced by the iterative reconstruction. The width of the median filter (Pratt 2017) was 3 pixels. For the bilateral filter (Petschnigg *et al* 2004), the distance deviation was 6 pixels, and the intensity deviation was 0.05. The parameters were adjusted to achieve the best performance.

3. Results

3.1. Dual-energy method

Dimensional measurement error results are shown in figure 5(a). Recall that errors are determined in relation to a monochromatic simulation. For reference, the errors for two polychromatic simulations (at 50 kVp and 70 kVp) without beam hardening correction are shown in figure 4. The experiment shows that the errors present in the 50 kVp and 70 kVp uncorrected reconstructions are significantly reduced when the dual-energy method can rely on the original spectra. However, the performance of the method is impaired by the absence of accurate spectral information: the dataset reconstructed with the approximated spectra yields errors whose absolute values are even larger than those without correction. A line profile of an Al rod is shown in figure 5. The shape of the simulated spectrum (blue dashed line) is more sloped at the edge position of the rod. The artefact reduction indices are presented in table 3. The artefacts are largely reduced both with the approximated and the actual spectral information. Yet the results show that the appearance of the cupping effects and streaks with the approximated spectra is about twice as strong as that of the true spectra. The pictorial demonstration of the artefact reduction is given in figure 6. More streaks can be clearly seen in the image reconstructed with the approximated spectra.

3.2. Segmentation based linearisation method

Dimensional measurement error results are shown in figure 7(a). Unlike the dual-energy algorithm, which employs two datasets to produce one pseudo-monochromatic dataset, the segmentation method and iterative method act upon single dataset. Therefore, the 50 and 70 kVp are processed individually with the approximated and true spectra. In both cases, the dimensional measurement errors are considerably reduced after BHC, when using the true spectra as well as when relying on approximated spectra. Although the dimensional measurement errors are smaller in the true spectra processed datasets for both 50 and 70 kVp, the distinction is not as substantial as in the dual-energy result. Moreover, all the dimensional measurement errors are under $2 \mu\text{m}$. Line profiles are shown in

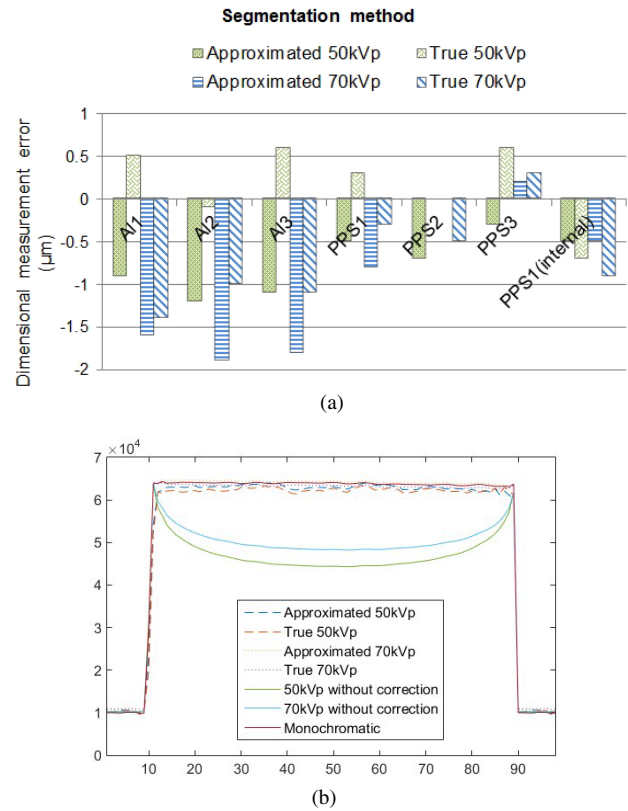


Figure 7. Segmentation based linearisation method.

(a) Dimensional measurement errors obtained from uncorrected polychromatic simulations (no correction), from the simulation using the same spectra for forward projection and for segmentation BHC (True), and from the simulation using different spectra for forward projection and for segmentation BHC (Approximated). All errors are defined with respect to the monochromatic simulation.

(b) Line profiles along a diameter of rod Al₁ obtained from the monochromatic simulation, the uncorrected polychromatic simulations, from the simulation using the true spectra for segmentation BHC, and from the simulation using the approximated spectra.

figure 7(b). The line profiles stemming from all beam hardening corrected reconstructions look similar despite the spectral changes. However, the line profiles of the segmentation datasets are slightly more irregular than the dual-energy ones. This indicates that dual-energy yields better material uniformity than the segmentation method. The artefact reduction indices are presented in table 3. All SI values equal 0. This implies the segmentation method was able to eliminate all streaks in the defined ROI, and that the performance was not degraded with spectral deviations. The CI values are negligible for all segmentation BHC reconstructions, regardless of whether true or approximated spectra were used. The pictorial demonstration of the artefact reduction is given in figure 6.

3.3. Iterative reconstruction method

The results shown in figure 8(a) and table 3 indicate that the iterative method is superior in BHC reduction when targeting good image quality, and moreover robust with respect to spectral change. All line profiles are flat and smooth, indicating

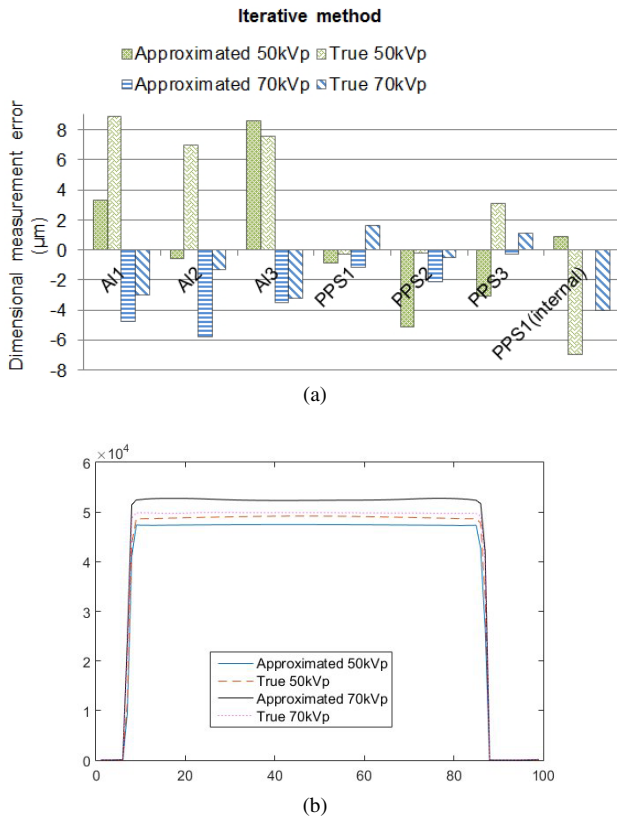


Figure 8. Iterative reconstruction method. (a) Dimensional measurement errors obtained the simulation using the same spectra for forward projection and for iterative BHC (True), and from the simulation using different spectra for forward projection and for iterative BHC (Approximated). All errors are defined with respect to the monochromatic simulation. (b) Line profiles along a diameter of rod Al₁ obtained from the simulation using the true spectra for iterative BHC, and from the simulation using the approximated spectra.

that there is no cupping effect, and the material uniformity is good. The minor slopes at the edge of the rod are likely to be caused by the bilateral filter applied to the dataset. The SI values equal 0, and the CI values are negligible for BHC reconstructions using both true and approximated spectra. Figure 8(a) depicts the dimensional measurement error results. This result looks less promising than the former ones. The iterative dataset seems to yield more variation dimensionality-wise. This rather contradictory result may be due to the post-filtration we applied to the datasets. Indeed, any filter would tend to suppress the edge (high frequency) to some extent. Notice that the ‘No correction’ plotted in the previous sections are not presented here. This is because those are FBP reconstructed datasets, whereas the iterative method itself is a reconstruction algorithm with a different mathematical model. The pictorial demonstration of the artefact reduction is given in figure 6.

4. Discussion and conclusions

In this study, we have tested the effects of spectral variation on the performance of three BHC algorithms. We quantified the uncertainties caused by spectral deviations. The dual-energy

method performed well when the spectral information was available as *a priori* knowledge. When the spectral information was not available, it managed to show a certain degree of improvement compared to the polychromatic datasets without BHC with respect to image artefacts, yet the performance was considerably weakened with respect to dimensional measurements. The segmentation method and iterative method performed equally well in artefact reduction. The latter method gave better material uniformity, whereas the former was more stable in dimensional measurement.

From our earlier observations of the dual-energy method (Cao *et al* 2018), the dual-energy method was extremely sensitive to the characteristic peaks of the spectra. The removal or even a slight location shift of a characteristic peak can result in a prominent change in the performance. From figure 2(b) we can see the peaks of the true 70 kVp spectrum were not presented in the approximated spectrum. This might be the reason for the severe performance degradation of the dual-energy method.

One drawback of the segmentation-based linearisation method was the visual quality. The low contrast visibility was worse than that of the other two methods. In addition, although cupping effects were alleviated, the line profile of the segmentation method showed more oscillation than in the other two methods. This was an indication of lower material uniformity. The segmentation method evaluated the initial reconstruction volume, estimated integral dependent non-linearity for each pixel, and then re-projected the image. There were several steps involved in this process and the errors can accumulate. These errors introduced noise to the final reconstruction image. Dual-energy and iterative methods needed no such process since they inherently accounted for the nonlinearities. It seems possible that this is the reason for the worse visual quality of the segmentation method.

The iterative method was able to achieve relatively good performance with the aid of post-filtration. However, this process required empirical trial-and-error experimentation. In addition, as the filtration changed the edge profile of the reconstructed image, it introduced extra uncertainty to the edge detection and subsequently dimensional measurement.

In summary, when the true spectra of a CT system are available, the dual-energy method is a suggested solution to beam hardening, as it works well both visually and dimensionally. However, more commonly only the approximated spectra are applicable. On the comparison of the visual quality, it is clear that the iterative method is the preferable one. The segmentation method, on the other hand, is more trustworthy in dimensional measurements.

In practice, scattering produces artefacts that look similar to beam hardening artefacts. As the methods discussed in this paper are only effective in reducing beam hardening, there will be remaining artefacts in the real scanning datasets. The performance of the algorithms will, therefore, be degraded from this simulation study. In spite of its limitations, the study certainly adds to our understanding of the BHC algorithms with regards to the performance change over spectral deviation. An extended study based on real scanning datasets and measured detector spectra of the corresponding CT system

would allow us to explore the role of scattering. This includes manufacturing of the phantom, projection data acquisition, and spectral estimation of the CT system. Recently, investigations on the combined impact of scattering and beam hardening (Lifton and Carmignato 2017) and scattering correction aided BHC (Lee and Chen 2015) are emerging. With the insights provided in these studies, this would be a fruitful area for further work.

Acknowledgment

This work has received funding from the European Union's Seventh Framework Programme under grant agreement No. 607817. We would like to express our thanks to Dr Heather Durko of Nikon Research Corporation of America for providing the implementation of the Alvarez algorithm.

ORCID iDs

Wenchao Cao  <https://orcid.org/0000-0001-6437-5096>

References

- Abella M and Fessler J A 2009 A new statistical image reconstruction algorithm for polyenergetic x-ray CT *IEEE Int. Symp. on Biomedical Imaging: from Nano to Macro* (IEEE) pp 165–8
- Alvarez R E and Macovski A 1976 Energy-selective reconstructions in x-ray computerised tomography *Phys. Med. Biol.* **21** 733
- Bellon C and Jaenisch G R 2007 Artist-analytical rt inspection simulation tool *Proc. DIR* pp 25–7 (<https://www.ndt.net/article/wcndt2008/papers/64.pdf>)
- Birch R and Marshall M 1979 Computation of bremsstrahlung x-ray spectra and comparison with spectra measured with a Ge (Li) detector *Phys. Med. Biol.* **24** 505
- Brabant L, Pauwels E, Dierick M, Van Loo D, Boone M and Van Hoorebeke L 2012 A novel beam hardening correction method requiring no prior knowledge, incorporated in an iterative reconstruction algorithm *NDT E. Int.* **51** 68–73
- Bushberg J T and Boone J M 2011 *The Essential Physics of Medical Imaging* (Baltimore, MD: Williams and Wilkins)
- Cao W, Fardell G, Price B and Dewulf W 2018 Simulation based study on the influence of deviations between the assumed and actual x-ray spectra on the performance of the Alvarez dual-energy method for beam-hardening correction *NDT* (https://www.ndt.net/article/ctc2018/papers/ICT2018_paper_id168.pdf)
- de Castele E V, Van Dyck D, Sijbers J and Raman E 2004 A model-based correction method for beam hardening artefacts in x-ray microtomography *J. X-Ray Sci. Technol.* **12** 43–57
- De Man B, Nuyts J, Dupont P, Marchal G and Suetens P 2001 An iterative maximum-likelihood polychromatic algorithm for CT *IEEE Trans. Med. Imaging* **20** 999–1008
- Duan X, Wang J, Yu L, Leng S and McCollough C H 2011 CT scanner x-ray spectrum estimation from transmission measurements *Med. Phys.* **38** 993–7
- Fessler J A, Elbakri I, Sukovic P and Clinthorne N H 2002 Maximum-likelihood dual-energy tomographic image reconstruction *Proc. DIR* (SPIE) (<https://doi.org/10.1117/12.467189>)
- Gao H, Zhang L, Chen Z, Xing Y and Li S 2006 Beam hardening correction for middle-energy industrial computerized tomography *IEEE Trans. Nucl. Sci.* **53** 2796–807
- Herman G T 1979 Correction for beam hardening in computed tomography *Phys. Med. Biol.* **24** 81
- Herman G T 2009 *Fundamentals of Computerized Tomography: Image Reconstruction from Projections* (Berlin: Springer)
- Herman G T and Trivedi S S 1983 A comparative study of two postreconstruction beam hardening correction methods *IEEE Trans. Med. Imaging* **2** 128–35
- Hsieh J, Molthen R C, Dawson C A and Johnson R H 2000 An iterative approach to the beam hardening correction in cone beam CT *Med. Phys.* **27** 23–9
- Jacobs F, Sundermann E, De Sutter B, Christiaens M and Lemahieu I 1998 A fast algorithm to calculate the exact radiological path through a pixel or voxel space *CIT J. Comput. Inf. Technol.* **6** 89–94 (<http://users.elis.ugent.be/~brdsutte/research/publications/1998JCITjacobs.pdf>)
- Joseph P M 1982 An improved algorithm for reprojecting rays through pixel images *IEEE Trans. Med. Imaging* **1** 192–6
- Joseph P M and Ruth C 1997 A method for simultaneous correction of spectrum hardening artifacts in CT images containing both bone and iodine *Med. Phys.* **24** 1629–34
- Joseph P M and Spital R D 1978 A method for correcting bone induced artifacts in computed tomography scanners *J. Comput. Assist. Tomogr.* **2** 100–8
- Kerckhofs G 2009 Morphological and mechanical quantification of porous structures by means of micro-ct *PhD Thesis* Katholieke Universiteit Leuven (https://limo.libis.be/primo-explore/fulldisplay?docid=LIRIAS1752961&context=L&vid=Lirias&search_scope=Lirias&tab=default_tab&lang=en_US)
- Krumm M, Kasperl S and Franz M 2008 Reducing non-linear artifacts of multi-material objects in industrial 3d computed tomography *NDT E. Int.* **41** 242–51
- Lee J S and Chen J C 2015 A single scatter model for x-ray CT energy spectrum estimation and polychromatic reconstruction *IEEE Trans. Med. Imaging* **34** 1403–13
- Leinweber C, Maier J and Kachelrieß M 2017 X-ray spectrum estimation for accurate attenuation simulation *Med. Phys.* **44** 6183–94
- Lifton J 2017 Multi-material linearization beam hardening correction for computed tomography *J. X-Ray Sci. Technol.* **25** 629–40
- Lifton J and Carmignato S 2017 Simulating the influence of scatter and beam hardening in dimensional computed tomography *Meas. Sci. Technol.* **28** 104001
- Lin Y, Ramirez-Giraldo J C, Gauthier D J, Stierstorfer K and Samei E 2014 An angle-dependent estimation of CT x-ray spectrum from rotational transmission measurements *Med. Phys.* **41**
- Meagher J, Mote C and Skinner H 1990 CT image correction for beam hardening using simulated projection data *IEEE Trans. Nucl. Sci.* **37** 1520–4
- Miyajima S, Imagawa K and Matsumoto M 2002 CdZnTe detector in diagnostic x-ray spectroscopy *Med. Phys.* **29** 1421–9
- Nalcioglu O and Lou R 1979 Post-reconstruction method for beam hardening in computerised tomography *Phys. Med. Biol.* **24** 330
- Petschnigg G, Szeliski R, Agrawala M, Cohen M, Hoppe H and Toyama K 2004 Digital photography with flash and no-flash image pairs *ACM Trans. Graph.* **23** 664–72
- Poludniowski G, Landry G, DeBlois F, Evans P and Verhaegen F 2009 Spekcalc: a program to calculate photon spectra from tungsten anode x-ray tubes *Phys. Med. Biol.* **54** N433
- Pratt W K 2017 *Digital Image Processing: College Edition* (New York: Wiley)

- Redus R H, Pantazis J A, Pantazis T J, Huber A C and Cross B J 2009 Characterization of CdTe detectors for quantitative x-ray spectroscopy *IEEE Trans. Nucl. Sci.* **56** 2524–32
- Siddon R L 1985 Prism representation: a 3d ray-tracing algorithm for radiotherapy applications *Phys. Med. Biol.* **30** 817
- Sidky E Y, Yu L, Pan X, Zou Y and Vannier M 2005 A robust method of x-ray source spectrum estimation from transmission measurements: demonstrated on computer simulated, scatter-free transmission data *J. Appl. Phys.* **97** 124701
- Siewerdsen J, Waese A, Moseley D, Richard S and Jaffray D 2004 Spektr: a computational tool for x-ray spectral analysis and imaging system optimization *Med. Phys.* **31** 3057–67
- Stumbo S, Bottigli U, Golosio B, Oliva P and Tangaro S 2004 Direct analysis of molybdenum target generated x-ray spectra with a portable device *Med. Phys.* **31** 2763–70
- Van Slambrouck K and Nuyts J 2012 Metal artifact reduction in computed tomography using local models in an image block-iterative scheme *Med. Phys.* **39** 7080–93
- Zbijewski W and Beekman F J 2003 Characterization and suppression of edge and aliasing artefacts in iterative x-ray CT reconstruction *Phys. Med. Biol.* **49** 145
- Zhang R, Thibault J B, Bouman C A, Sauer K D and Hsieh J 2014 Model-based iterative reconstruction for dual-energy x-ray CT using a joint quadratic likelihood model *IEEE Trans. Med. Imaging* **33** 117–34